The Global S_1 Tide

RICHARD D. RAY

Laboratory for Terrestrial Physics, NASA Goddard Space Flight Center, Greenbelt, Maryland

GARY D. EGBERT

College of Oceanic and Atmospheric Sciences, Oregon State University, Corvallis, Oregon

ABSTRACT

The small S_1 ocean tide is caused primarily by diurnal atmospheric pressure loading. Its excitation is therefore unlike any other diurnal tide; in particular, pressure loading is maximum near the equator where the diurnal gravitational potential is zero. The global character of the S_1 tide is here determined by numerical modeling and by analysis of Ocean Topography Experiment (TOPEX)/Poseidon satellite altimeter data. The two approaches yield reasonably consistent results. Amplitudes exceeding 1 cm in several regions are further confirmed by comparison with coastal tide gauges. Notwithstanding their excitation differences, S_1 and other diurnal tides are found to share several common features, such as relatively large amplitudes in the Arabian Sea, the Labrador Sea, the Sea of Okhotsk, and the Gulf of Alaska. The most noticeable difference is the lack of an S_1 Antarctic Kelvin wave. These similarities and differences can be explained in terms of the coherences between near-diurnal oceanic normal modes and the underlying tidal forcings. Whereas gravitational diurnal tidal forces excite primarily a 28-h Antarctic–Pacific mode, the S_1 air tide excites several other near-diurnal modes, none of which has large amplitudes near Antarctica.

1. Introduction

It has long been known that the ocean has a small tide occurring at exactly the frequency of 1 cycle per solar day. Its amplitude exceeds 1 cm in only a few locations. It has also long been known that this tide, denoted S_1, is anomalous: unlike other diurnal tides it cannot be driven by the gravitational tidal potential because the potential at the S_1 frequency is minuscule. The tide is also anomalous because some ''observations'' of it are nothing more than the manifestation of systematic error. The daily heating and cooling of a tide gauge, or any other thermally sensitive instrument, make direct measurements less reliable than one would like and uncertainties in tidal estimation difficult to assess.

To the extent that it is real, the S_1 tide is an example of a ''meteorological'' tide (e.g., Schureman 1940). It may also be classified a ''radiational'' tide, in the sense of Munk and Cartwright (1966), because its ultimate cause is insolation. The direct, immediate forcing of S_1 appears to be predominantly ocean loading by the S_1 atmospheric pressure tide. In some coastal areas, diurnal sea breezes may also be contributory. Diurnal thermal expansion of the water column is of little importance.

Partly because of the smallness of the tide, and partly owing to the associated instrumental errors, there has, to our knowledge, never been a published global chart of S_1. (F. Lyard and L. Carrère have recently computed a finite-element hydrodynamic solution of S_1, with forcing equivalent to our Fig. 1 below; F. Lyard and L. Carrère 2003, personal communication.) Why should such a small tide now attract our detailed attention? We offer three reasons. 1) Owing to its unique excitation, one expects the S_1 tide to look like no other diurnal tide. Whether this is so or not, it gives us the opportunity to study the ocean's response to markedly different forcings of nearly identical frequency. 2) The S_1 tide acts as a small additional (internal) excitation to the earth's prograde annual nutation. Theory and observation of this nutation have long been discordant (Mathews et al. 2002), and a better accounting of the ocean's contribution may help to resolve this issue. 3) As geodetic measurements grow ever more precise, they put additional demands on tidal models. For some applications S_1 is sufficiently large that it can no longer be ignored (Ponte and Ray 2002).

Our first goal here is to establish, in a possibly gross sense, the global character of the S_1 tide. Because of the possibly overwhelming influence of systematic measurement errors in empirical determinations of S_1, we adopt a two-pronged, complementary approach, con-

Corresponding author address: Richard D. Ray, NASA/GSFC, Code 926, Greenbelt, MD 20771.
E-mail: richard.ray@gsfc.nasa.gov

sisting of data analysis and of numerical hydrodynamic modeling. The primary data are 10 yr of Ocean Topography Experiment (TOPEX)/Poseidon (T/P) satellite altimetry. Of course, satellite altimetry is just as sensitive, perhaps even more sensitive, as any other instrument to systematic errors at once per solar day. This requires us to reexamine standard altimeter processing methods, some of which are clearly problematic for errors at the S_1 frequency; reducing such errors is crucial.

In the end the two approaches—modeling and data analysis—are found to agree in many respects, which lends confidence to both solutions. A surprising finding is the degree to which S_1 mimics the behavior of other gravitational diurnal tides. A common characteristic, for example, is relatively large tides in the Arabian Sea, the Okhotsk Sea, the Labrador Sea, and the Gulf of Alaska. They differ, however, in that S_1 displays no hint of an Antarctic Kelvin wave, which is a well-known feature of nearly all diurnal tides (e.g., Cartwright and Ray 1991). Much of this can be understood in terms of oceanic normal modes. A small number of modes resonant near the diurnal frequency dominate the ocean response, resulting in similarities for all diurnal tides. However, the degree to which individual modes are excited depends on the spatial forcing pattern, leading to differences between S_1 and other diurnal tides.

The next section discusses the possible forcing mechanisms for the S_1 tide. This is followed by a discussion of T/P satellite solutions and then by numerical modeling solutions. Section 5 compares these solutions with selected tide gauge estimates. Section 6 presents further analysis of the S_1 tide, as well as other diurnal tides, and addresses their relative excitations in terms of normal-mode theory.

This paper is not the proper vehicle for an extended discussion of nutation. We do, however, take the opportunity to tabulate (in appendix B) the global angular momentum integrals from our S_1 ocean model. With this information future nutation modeling may more rigorously account for the ocean's contribution.

2. Generation mechanisms for the S_1 tide

This section reviews the various possible mechanisms that can generate oscillations in sea level at the S_1 frequency. The dominant mechanism is evidently ocean pressure loading by the S_1 atmospheric tide, but other mechanisms are also possibly important in some locations.

a. Atmospheric pressure loading

The diurnal S_1 atmospheric tide is driven by the daily variation in insolation; the gravitational tidal potential at S_1 is of no significance (see below). The primary generation mechanism is heat absorption by tropospheric water vapor and upper-level ozone and boundary layer heating over large land masses; there are other sec-

ondary mechanisms as well (e.g., Forbes 1982). At the earth's surface, pressure oscillations associated with the diurnal tide are of order 1 mbar. They have a rather complicated spatial pattern with higher amplitudes over some landmasses and lower amplitudes over the ocean (e.g., Chapman and Lindzen 1970; Haurwitz and Cowley 1973; Dai and Wang 1999).

In this paper we employ a quasi-empirical model of the S_1 barometric tide that was deduced by Ray and Ponte (2003) from 13 yr of global surface pressure fields produced on an operational basis by the European Centre for Medium-Range Weather Forecasts (ECMWF); see also Hsu and Hoskins (1989). Figure 1 shows the amplitude and Greenwich phase lag of this diurnal pressure wave. (For phase conventions, see appendix A.) According to Fig. 1, the largest amplitudes over the oceans are about 0.8 mbar and occur over the tropical Pacific Ocean. Comparison of the amplitudes and phases of Fig. 1 with a set of "ground truth" stations at which the S_1 tide is known from long time series of hourly barometer readings (Ray 1998) shows an rms discrepancy over ocean regions of only 68 μbar (Ray and Ponte 2003). The ECMWF tide has also been shown to be more accurate than the tide deduced from some other commonly available reanalysis products, which probably reflects on the relative accuracy of analysis versus reanalysis products (Ray and Ponte 2003).

An equilibrium ocean response to diurnal pressure loading of 1 mbar would generate a sea level anomaly of order 1 cm, which is approximately the observed magnitude of the S_1 ocean tide. Of course, the ocean's response to atmospheric loading is manifestly not equilibrium at the S_1 frequency—compare the well-known nonequilibrium behavior of gravitational diurnal tides. The dynamic response is modeled in detail in section 4.

The spatial pattern of the pressures in Fig. 1 is noticeably more complex than the smooth pattern of the gravitational tidal potential. More important, the long-wavelength character is completely different. The air tide field is, more or less, symmetric about the equator, while the diurnal gravitational potential, being a spherical harmonic function $Y_2^1(\theta, \varphi)$ of degree 2, order 1, is antisymmetric. The air tide over the ocean is maximum on the equator; the gravitational potential is zero at the equator and maximum at latitudes $\pm45°$. For these reasons we would expect the ocean's response to loading by the S_1 air tide to be markedly different from its response to gravitational diurnal tidal forcing. We explore this in more detail in section 6.

An important aspect of atmospheric tides, and particularly the diurnal tide, is their relatively large temporal variability (e.g., Haurwitz and Cowley 1973; Vial et al. 1994). Such variability is present in the ECMWF tide as well. Figure 2 shows the globally integrated spectrum of the ECMWF surface pressure time series (in this case, for 4 yr) in the near-diurnal frequency band. In addition to the fundamental peak at S_1, the spectrum shows significant energy at nearby frequencies, imply-
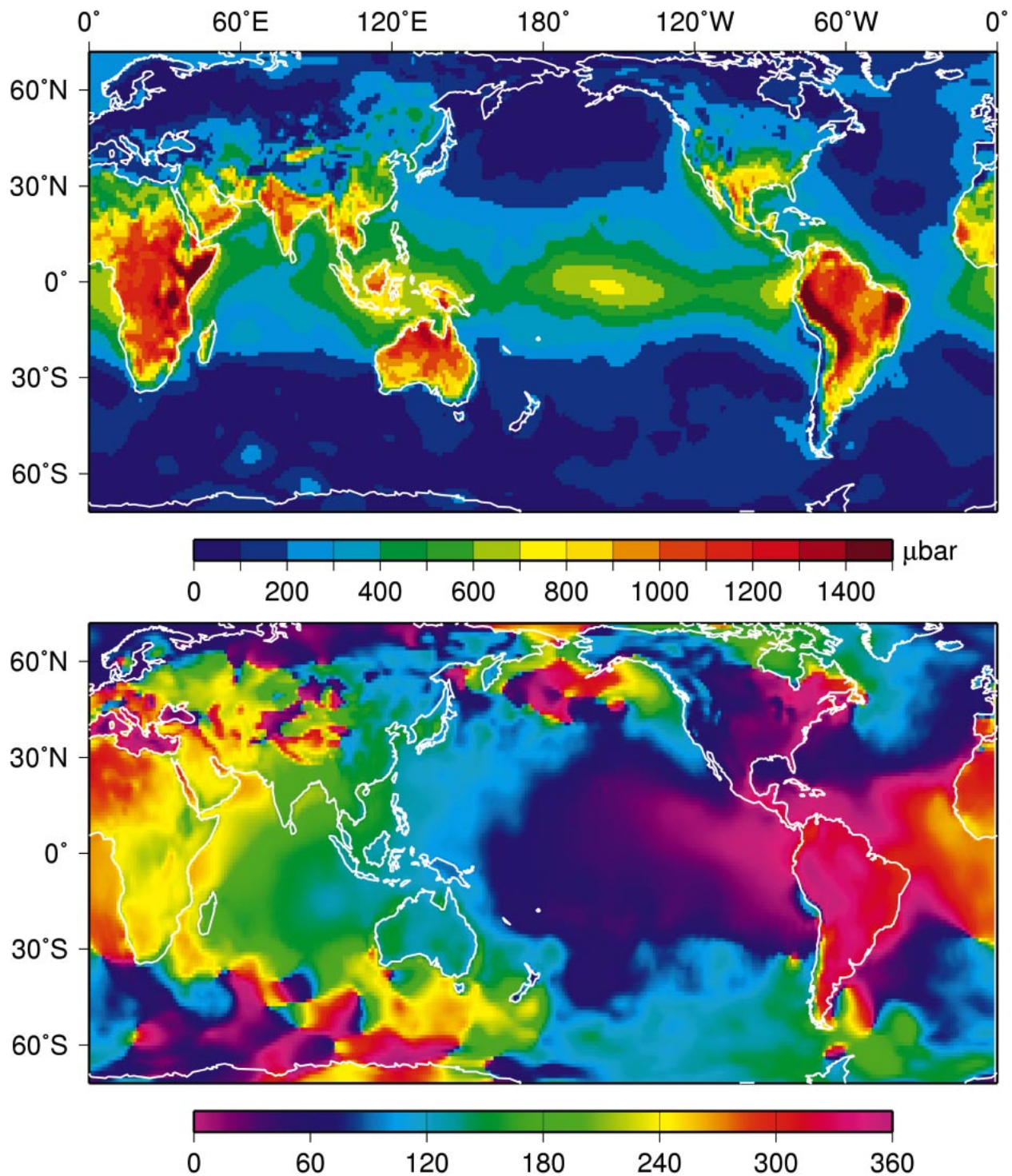
FIG. 1. (top) Amplitude and (bottom) Greenwich phase lags of the $S_1(p)$ atmospheric tide, as deduced from ECMWF surface pressures by Ray and Ponte (2003).

ing tidal variability at both interannual and intra-annual periods. Specifically, there are clear harmonics representing modulation of S_1 by integer multiples of 1 cpy, superimposed on a broad "cusp" of enhanced energy.

The ocean responds, of course, to all of this near-diurnal energy, but the present paper addresses only the central peak, occurring at precisely the S_1 frequency, that is, the mean S_1 tide. Note that the side peaks occur at
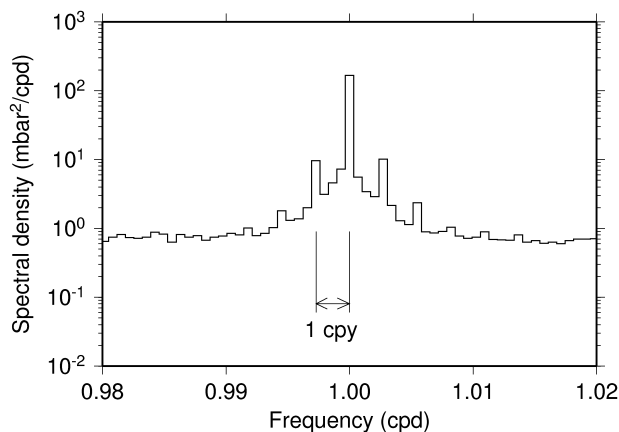
FIG. 2. Globally integrated spectrum of ECMWF surface pressures in the near-diurnal band of frequencies. Spectral resolution is 1 cycle $(4 \text{ yr})^{-1}$. The spectrum estimation technique, following Wunsch and Stammer (1995), is based on integrating a global frequency–wavenumber spectrum over all wavenumbers. The central peak corresponds to the frequency of the S_1 tide, and the side peaks represent seasonal modulations of S_1. The two peaks closest to S_1 also correspond to the frequencies of the P_1 and K_1 gravitational tides.

frequencies of other, primarily gravitational, tides and therefore represent some (relatively minor) radiational component to the forcing of those tides. For example, the lines immediately neighboring S_1 in Fig. 2 correspond to the P_1 and K_1 tides. Empirical models of P_1 and K_1 that are based on tidal observations would automatically include these small radiational components.

b. Wind stress

In addition to surface pressure waves, atmospheric tides have associated wind fields. These winds are impressively strong in the upper atmosphere. They are, for example, the dominant motion in the thermosphere (Dickinson 1975). At the ocean's surface they are weak. Recent studies have determined mean diurnal winds at the ocean surface of perhaps 0.3 m s^{-1} (Deser and Smith 1998; Dai and Deser 1999). The corresponding wind stress τ on the ocean is of order 10^{-4} Pa.

In the barotropic momentum equations the wind stress appears through a term such as $\tau/(\rho H)$, where ρ is seawater density and H is ocean depth, while the pressure appears through a term such as $\nabla P/\rho$, which scales as $(P/\rho L)$, where L is the length scale for pressure variations. For the S_1 atmospheric tide L is of order 10^4 km or smaller. Hence the pressure term $(P/\rho L)$ scales as 10^{-8} m s^{-2}, whereas the wind stress term is at least two orders of magnitude smaller. Evidently the atmospheric tide is more effective at generating S_1 sea level oscillations through its pressure loading than through its wind stress.

A possible exception to the importance of wind is in near-coastal areas where H is small and where persistent, diurnal, land–sea breezes can occur with speeds of order 1 m s^{-1}, and 10 times that in extreme cases (e.g., Pat-

tiaratchi et al. 1997). Winds of this magnitude could set up coastal sea level anomalies comparable to observed S_1 tidal amplitudes. However, these are very localized features in the global ocean, and we ignore them below in our dynamic modeling.

c. Gravitational

In the gravitational tidal potential (e.g., Cartwright and Tayler 1971; Cartwright and Edden 1973) the S_1 constituent comprises two very small spectral lines, separated in frequency by only 2 cycles in 21 000 yr. The amplitudes of these two lines are more than two orders of magnitude smaller than the primary potential line of the K_1 tide, and so they are weak indeed. Like the major diurnal tides, the gravitational potential associated with the two S_1 lines is proportional to $Y_2^1(\theta, \varphi)$. The time dependence of the two lines is given by

$$A_1 \cos(\omega t - p') + A_2 \cos(\omega t + p'), \qquad (1)$$

where $\omega t = T + 90°$, with T equivalent to universal time, and p' is the mean longitude of the solar perihelion. In the tidal potential [scaled to length units as in Cartwright and Tayler (1971)] the amplitudes are given by (Cartwright and Edden 1973)

$$A_1 = 1.02 \text{ mm} \quad \text{and} \quad A_2 = 2.89 \text{ mm},$$

while the main line of the nearby K_1 tide has an amplitude of 368.74 mm.

At the present time the longitude of the solar perihelion p' is approximately $282.94°$ (Simon et al. 1994), and it changes only $1.72° (100 \text{ yr})^{-1}$. So for times around the present the two lines in (1) may be combined as

$$1.98 \cos(\omega t + 295.66°).$$

This gravitational potential will generate a small S_1 tide, which can be easily estimated from the diurnal band admittance, or specifically from observations of the P_1 and/or K_1 tides, which are each only 1 cpy away from S_1 in frequency. Over such a small frequency span, one expects the ocean's admittance to be nearly constant. Thus the phases of all three tides will be nearly identical at any location, and the amplitude of S_1 (gravitational part) will be given approximately as the amplitude of K_1 scaled by 1.98/368.74. The K_1 tide exceeds 0.5-m amplitude in only a few regions of the globe (e.g., Gulf of Thailand, Sea of Okhotsk, a few locations along the coast of southern Alaska). It exceeds 2 m only in Shelikhov Bay, in the northern reaches of the Sea of Okhotsk (Kowalik and Polyakov 1998). Hence, excepting Shelikhov Bay, the gravitational component of S_1 cannot exceed but a few millimeters anywhere in the global ocean.

d. Thermal

Solar diurnal heating produces a strong warming at the ocean surface but very little at depth. Under light

winds there may be a 2° or 3° rise over a depth of about 1 m (e.g., Halpern and Reed 1976). Under stronger winds this heating is mixed downward to perhaps 10 m but is correspondingly reduced in amplitude to a fraction of a degree. The thermal expansion from such heating is minute and may be safely excluded as a contributory forcing to S_1 sea level oscillations.

3. Empirical estimates from satellite altimetry

Because of the small amplitude of the S_1 tide and the likely presence of systematic errors at the S_1 frequency, it is not a priori evident that realistic empirical estimates can be extracted from satellite altimeter data. This section describes our attempt to do so from approximately 10 yr (364 repeat cycles) of T/P altimetry. Another long time series of measurements from the European Remote Sensing *ERS-1, ERS-2,* and Envisat altimeter satellites is of little value for the present task because of their sun-synchronous orbits. We therefore rely exclusively on T/P data.

We use a variant of the altimetry data described by Koblinsky et al. (1999). These data have "standard" tidal corrections (Ray 1999) applied, which is satisfactory for our purposes because these corrections do not (as of yet) include an S_1 ocean tide. They do include the minute S_1 body tide, a response of the entire solid Earth to the small generating potential described in section 2c. For that purpose a Love number $h_2 = 0.609$ was used.

We employ a binning-type tidal analysis method, akin to that used by Schrama and Ray (1994) and others. The S_1 estimates thus result from a purely empirical analysis of the data, with no prior assumptions about dynamics and no prior model of S_1. We shall not repeat details of data processing insofar as they are standard (e.g., Koblinsky et al. 1999), but discussion of problems directly related to S_1 is necessary.

Some consideration must first be given to matters of aliasing. The 9.9156-day repeat of T/P aliases the S_1 tide to a period of 117.5 days. This is somewhat long, but is well away from the alias periods of all other major tides. One minor tide, the long-period Mt tide, has an alias of 115.7 days, which in principle requires about 20 yr to separate from S_1, but because Mt is a lunar tide the use of both ascending and descending tracks considerably reduces any correlation with S_1 over the course of our present 10-yr time series (see discussion in Schrama and Ray 1994).

Note that 117 days is also the period of the precession of the satellite orbit plane relative to the sun (the β' angle in orbit-theory parlance). This period is thus susceptible to errors in the computed satellite ephemeris, primarily from solar radiation forces. Although such errors are expected to be small because of the detailed nonconservative force modeling on T/P (Marshall and Luthcke 1994) and other empirical adjustments to the ephemeris (Marshall et al. 1995), we cannot rule out

contamination at the small level of the S_1 tide. There is some evidence (F. Lemoine 2003, personal communication) that such errors will manifest themselves primarily in the South Pacific where satellite tracking stations are sparse (or nonexistent).

For this analysis the standard correction for nontidal atmospheric loading requires special care. The altimetric variance associated with loading is large—second only to the tides—so it is crucial to apply this correction for general noise reduction, but it must be modified so as to remove the S_1 tide signal in the adopted atmospheric pressure fields. Allowing, for example, a standard "inverted barometer" correction to include the S_1 frequency not only entails use of a completely inaccurate model of the ocean's response at such high frequencies, it also in our case totally contaminates the signal of interest. We have therefore applied loading corrections based on an inverted barometer assumption but using daily mean pressure fields, which can have no power at the S_1 frequency. We have adopted the daily mean surface pressure fields from the National Centers for Environmental Prediction (NCEP)–National Center for Atmospheric Research (NCAR) reanalysis project (Kalnay et al. 1996).

Correction for the dry tropospheric delay (e.g., Koblinsky et al. 1999) also depends on pressure. In this case, however, we require the pressures to include the S_1 atmospheric tide, because S_1 induces a real tropospheric delay that must be compensated. Hence, the standard T/P correction (based on modified 6-h surface pressures from ECMWF) is retained.

Tropospheric delay errors could also arise from known diurnal signals in clouds, water vapor, and rainfall (Soden 2000; Wood et al. 2002). Corrections stemming from the satellite microwave radiometer compensates for some of these errors, and deletion of data collected near heavy rain cells is routinely performed. It is still conceivable that diurnally recurring rain events contaminate our S_1 results, either directly through distortion of the altimeter wave forms (Quartley et al. 1996) or indirectly through repeated data gaps at particular local times.

The main result of our analysis of the T/P data is Fig. 3, which shows the amplitudes and Greenwich phase lags of the resulting estimated S_1 tide, slightly smoothed with a median filter. At any location the standard error is of order 3–5 mm, somewhat larger in regions of high mesoscale variability. This level of estimation error appears fairly consistent with the noise level evident in the amplitude chart. Errors in phase are, of course, large in regions of small amplitude, and such errors are fairly obvious in the phase chart; phase patterns are most robust in regions of highest S_1 amplitudes. Large (i.e., exceeding 1 cm) S_1 amplitudes occur in the North Pacific, especially the Gulf of Alaska, the Sea of Okhotsk, the Arabian Sea, the eastern Indian Ocean, especially north of Australia, and the Labrador Sea.

Given the exceedingly weak excitation in high lati-
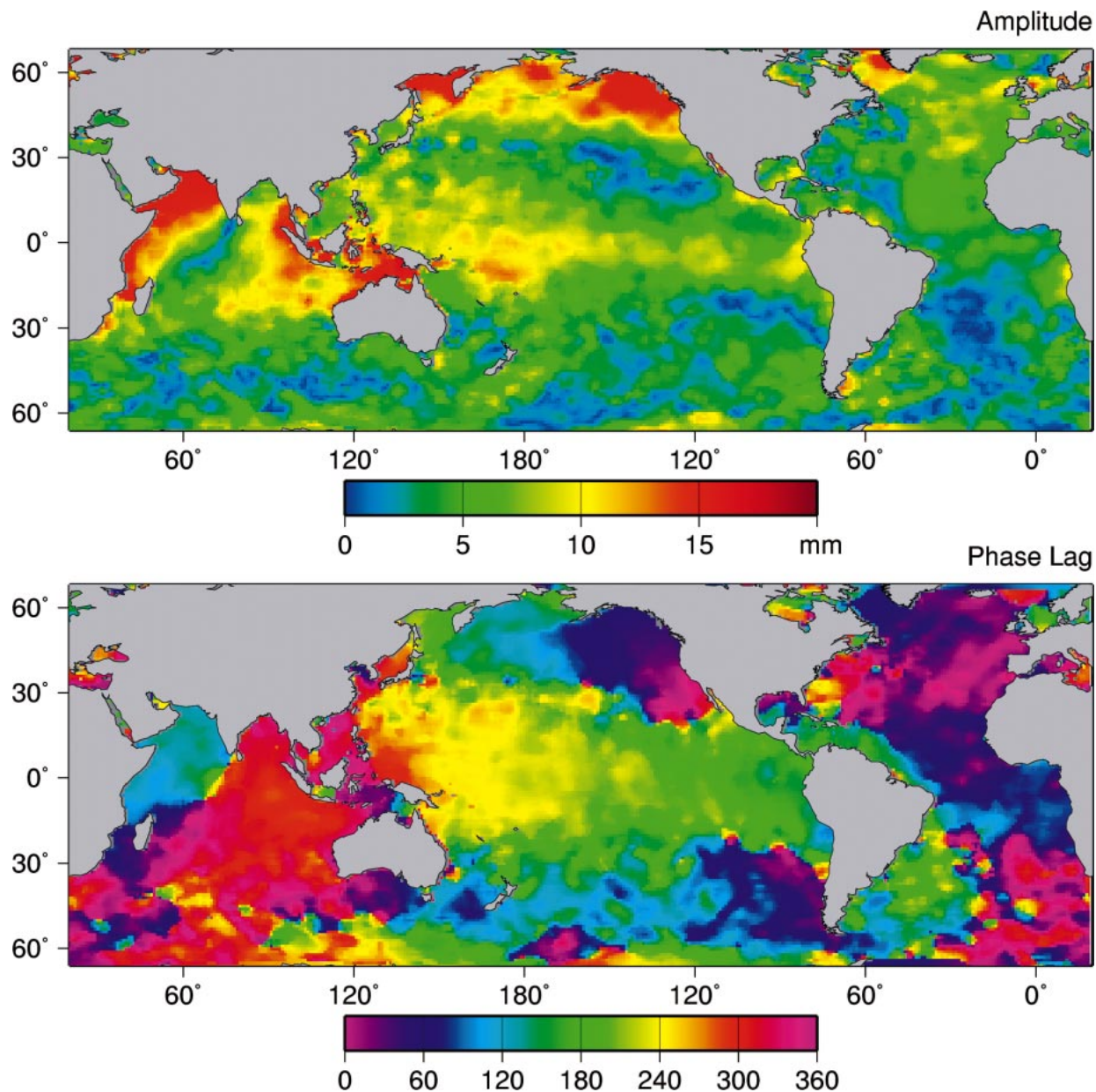
Amplitude

Phase Lag

FIG. 3. (top) Amplitude and (bottom) Greenwich phase lags of the S_1 ocean tide, as deduced from 10 yr of T/P altimeter measurements following methods essentially as in Schrama and Ray (1994). At any location the standard error is of order 3–5 mm. Some evident striping follows the satellite ground-track pattern.

tudes (see Fig. 1), the large S_1 amplitudes in the North Pacific, the Okhotsk Sea, and especially the Labrador Sea are surprising. We examine this point in some detail in section 6.

4. Numerical hydrodynamic solution for S_1

For comparison with Fig. 3 we have computed a numerical hydrodynamic S_1 solution, using the time-stepping barotropic model described by Egbert and Erofeeva (2002). The S_1 wave is forced by the surface pressure shown in Fig. 1 and by a self-attraction/loading term.

The two-dimensional momentum equations in this case are

$$\partial \mathbf{U}/\partial t + f\hat{z} \times \mathbf{U}$$
$$= -gH\boldsymbol{\nabla}(\zeta - P/g\rho - \zeta_{EQ} - \zeta_{SAL}) - \mathbf{F}/\rho, \quad (2)$$

where $\mathbf{U}$ is the volume transport vector, f is the Coriolis parameter oriented to the local vertical $\hat{z}$, g is gravitational acceleration, ρ is seawater density, H is water depth, ζ is the tidal surface displacement, ζ_{EQ} is the gravitational equilibrium tide, P is the S_1 atmospheric

pressure tide, and $\mathbf{F}$ is a frictional bottom stress evaluated as

$$\mathbf{F} = c\rho\|\mathbf{U}\|\mathbf{U}/H^2,$$

where the nondimensional drag coefficient c is taken as 0.003. We discuss ζ_{SAL} presently.

Equation (2), along with the corresponding continuity equation, was solved by time-stepping on a near-global C grid (latitude range 86°S–82°N) with grid resolution ¼°. The gravitational forcing included the major constituents M_2, S_2, N_2, and O_1. We used a time step of 22 s for 81 days, harmonically analyzing the last 69 days to determine the tidal constants of S_1. With this analysis window it was necessary to omit K_1 and P_1 from the forcing to prevent leakage into the S_1 constants. The gravitational forcing for S_1 was also omitted because, by inference from K_1, the S_1 gravitational component (see section 2c) is less than 3 mm everywhere.

The term ζ_{SAL} in (2) accounts for ocean tidal self-attraction and crustal loading (Hendershott 1972). It is computed from the (unknown) elevations ζ by convolution with a known kernel function, which thus transforms (2) into an integrodifferential equation that must be solved by iteration. In general there is no guarantee of convergence (Hendershott 1972), but rewriting the convolution in terms of a simplified scalar factor of ζ plus a correction term involving convolution (Accad and Pekeris 1978) does, we find, generally lead to convergence; for details see Egbert et al. (2004). We have solved (2) with and without the ζ_{SAL} complication, and we find (as have others, e.g., Gordeev et al. 1977) that the term is necessary to obtain a realistic solution in a global domain. Last, note that there is also a load deformation and associated potential induced by the air tide; it is much smaller than the likely errors in P and we neglect it.

Figure 4 shows the resulting S_1 tidal elevation charts. Being free of measurement error, this figure is, of course, much smoother than the satellite results shown in Fig. 3. Yet the two figures are reassuringly similar: relatively large amplitudes generally occur in similar locations and in those locations the phases are roughly equal. Phases are dissimilar in regions of low amplitude, but this again simply reflects the difficulty of empirically determining phase in weak signals and such discrepancies are of no importance. In fact, once the amplitudes are above just a few millimeters, the phase charts are in reasonably good agreement. The hydrodynamic amplitudes in the Gulf of Alaska are somewhat weaker than in the satellite solution; interestingly, a hydrodynamic solution without the ζ_{SAL} term in Eq. (2) is weaker still. Other regions of discrepancy include the Bering Sea and the central Pacific region near 10°S, 170°E, where the satellite amplitudes are significantly greater. It is conceivable that the latter area reflects errors in the altimetric solutions from liquid water, but this hypothesis is difficult to test. As an overall, quantitative summary, the global (complex) correlation coefficient between the two S_1 charts

is $0.73 - 0.07i$, which is reasonably consistent with our stated noise levels and a global rms (model) signal of about 6 mm. We conclude that, for such small signal, there is relatively good agreement between the altimeter and hydrodynamic solutions, which therefore lends credence to both.

A tidal ellipse chart for the S_1 volume transports is shown in Fig. 5. The largest transports are in the Indian Ocean. In keeping with the overall smallness of the S_1 tide, currents are generally weak everywhere, roughly 1/50 as strong as currents for the K_1 tide.

5. S_1 at selected tide gauges

As further confirmation of the basic structure of the S_1 cotidal charts we have examined some tide gauge estimates in selected regions where Figs. 3 and 4 show relatively large amplitudes. Some of these S_1 estimates have been extracted from the datasets of Ponchaut et al. (2001), and the remainder have been computed by us from multiyear time series of hourly tide gauge data. None of these measurements are from bottom pressure recorders, which would be directly sensitive to the air tide as well as the sea tide.

The tide gauge estimates are compiled in Table 1. We also list two gauges from the North Atlantic where Figs. 3 and 4 suggest low S_1 amplitudes.

Standard errors for the tidal estimates, although not shown in Table 1, were computed based on a combination of analyses of residual power spectra and of variability in multiple yearly estimations (for details see Ponchaut et al. 2001). At all stations the standard errors are in the range 0.5–1 mm, except for Karachi where the standard error is 2 mm.

In general the tide gauge estimates confirm the overall patterns observed in the altimetry and the modeling. In the Gulf of Alaska the gauges agree more closely with the model; the satellite amplitudes are about 50% larger at three sites although agreement is good at Prince Rupert. Interestingly, both satellite and model phases depict clear northward propagation, but the tide-gauge phases are more erratic.

Along the northwest coast of Australia the tide-gauge amplitudes are unusually large. The observed S_1 amplitude at Darwin is extraordinarily large, nearly 6 cm. The time series at Darwin includes periods with two different types of tide gauges, a traditional float mechanism and a modern acoustic gauge. We analyzed data from both gauges, and we find that they give consistent S_1 estimates, and so the large amplitude there is presumably not an instrumental artifact, but it could be very localized to the vicinity around Darwin. There is a sea breeze at Darwin, but it is not especially intense—about 1.5 m s^{-1} at the local airport.

6. Discussion

In many respects the S_1 tide, as depicted in Figs. 3 and 4, is similar to other diurnal tides, which is sur-
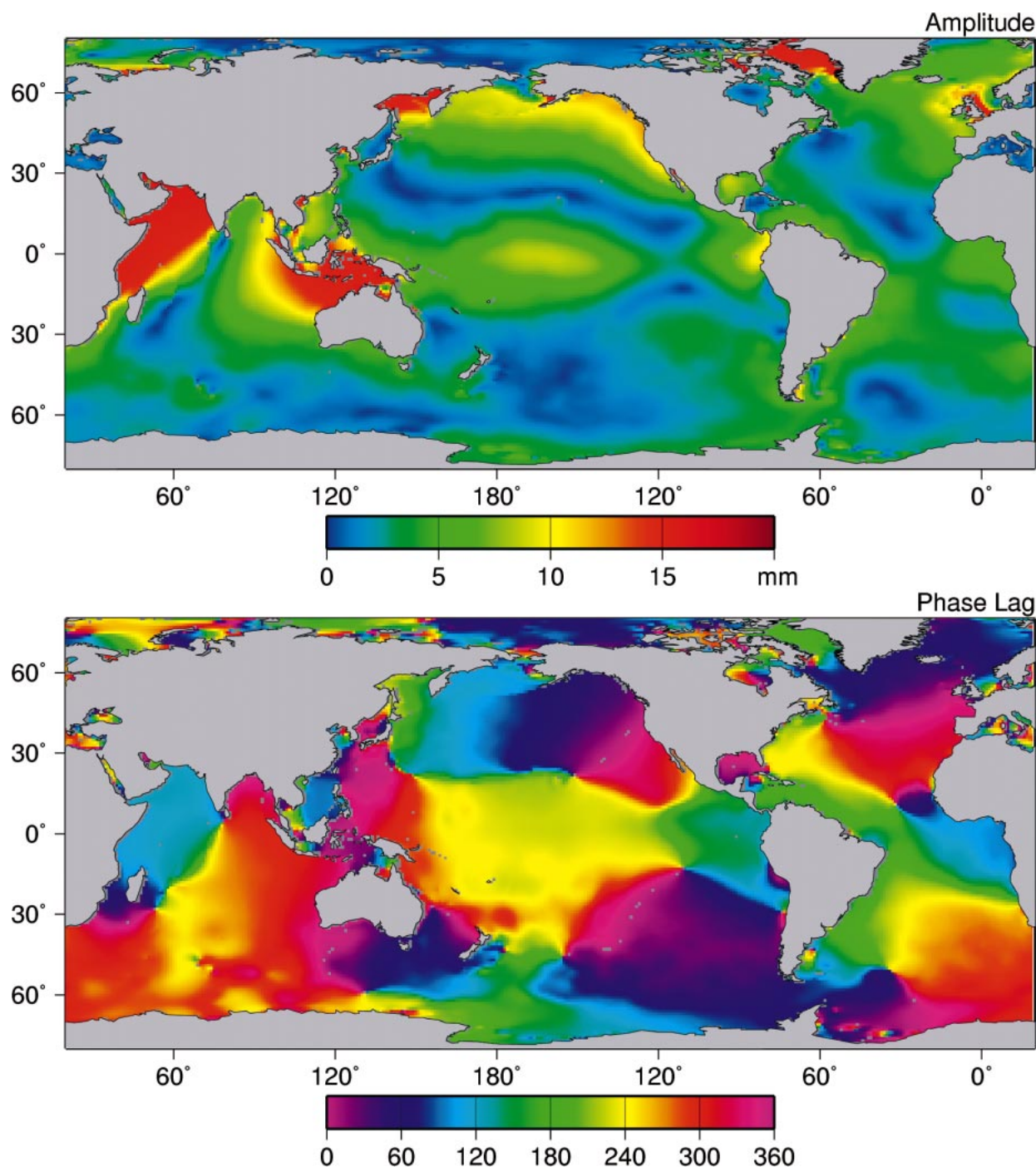
FIG. 4. (top) Amplitude and (bottom) Greenwich phase lags of the S_1 ocean tide as computed from the iterative time-stepping model described in section 4.

prising given the dissimilarity in spatial patterns of their forcings. For example, Fig. 6 is a modern determination of the K_1 tide, the principal declinational tide, and like S_1 it shows large amplitudes in the Arabian Sea, the Gulf of Alaska, the Gulf of Okhotsk, and so on. The major differences are 1) relatively larger S_1 amplitudes in the seas surrounding Indonesia and northwest Aus-

tralia, extending partially into the western equatorial Pacific and 2) the lack of an S_1 Antarctic Kelvin wave. In this section we address these similarities and differences in the context of normal-mode theory.

In a justly famous series of papers 20 years ago, Platzman computed the normal modes of the global barotropic ocean and laid out a procedure to use such modes
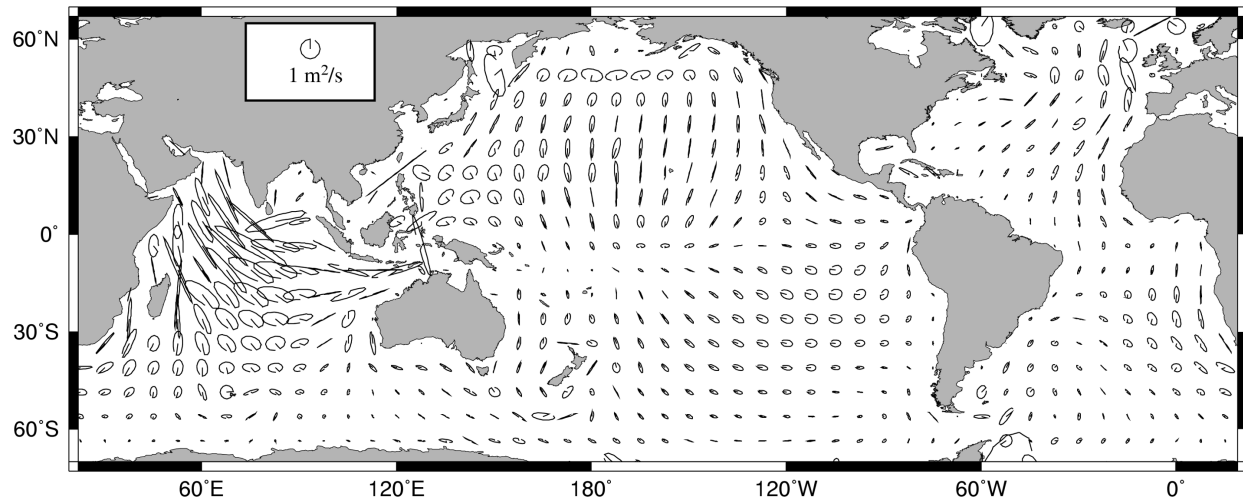
FIG. 5. Tidal ellipses for S$_1$ tide volume transports (current velocity $\times$ water depth). For plotting purposes ellipses are highly subsampled; the original grid resolution was ¼°.

for tidal synthesis (Platzman et al. 1981; Platzman 1984a,b, 1985). We here use Platzman's computed modes, not for realistic tidal synthesis, which was the goal of section 4, but rather to help to gain insight into the global characteristics of S$_1$ vis-à-vis K$_1$.

Let $\zeta(\omega, L)$ be the (complex) elevation amplitude of a tidal constituent of frequency ω at location L. We suppose that $\zeta(\omega, L)$ can be expressed as a series of oceanic normal modes k of complex amplitudes $H_k(L)$ and complex frequencies σ_k (Platzman 1991):

$$\zeta(\omega, L) = \sum_k (1 - \omega/\sigma_k)^{-1} S_k H_k(L), \qquad (3)$$

TABLE 1. Estimates of S$_1$ at selected tide gauges. Amplitudes A are in millimeters, phase lags G are in degrees, and phase convention follows appendix A.

Station	Latitude	Longitude	Timespan	Tide gauge		Satellite		Model	
				A	G	A	G	A	G
Northwest Australia									
Darwin*	12°28′S	130°51′E	1985–94	58.5	26°	45	35°	29	31°
Broome	18°00′S	122°13′E	1992–97	32.5	337°	18	336°	21	328°
Point Hedland	20°19′S	118°34′E	1987–99	36.9	329°	19	331°	19	331°
Indonesia									
Padang	1°00′S	100°22′E	1987–89	12.0	306°	15	299°	14	296°
Benoa	8°45′S	115°13′E	1988–90	17.1	339°	7	319°	19	319°
Arabian Sea									
Karachi	24°48′N	66°58′E	1988–92	26.5	95°	23	121°	25	118°
Masirah	20°41′N	58°52′E	1997–99	24.7	118°	21	140°	26	117°
Salalah*	16°56′N	54°00′E	1989–97	19.1	119°	21	135°	23	119°
East Africa									
Lamu	2°16′S	40°54′E	1995–2000	21.2	116°	16	127°	22	105°
Zanzibar*	6°09′S	39°11′E	1985–97	22.8	94°	18	107°	21	107°
Gulf of Alaska									
Yakutat*	59°33′N	139°44′W	1992–97	11.4	41°	17	54°	12	41°
Sitka	57°03′N	135°20′W	1950–2001	11.3	32°	18	52°	11	35°
Ketchikan	55°20′N	131°38′W	1949–97	11.7	53°	17	47°	12	33°
Prince Rupert*	54°19′N	130°20′W	1995–97	12.0	44°	12	32°	12	27°
Labrador Sea									
Iluslissat*	69°13′N	51°06′W	1992–95	14.6	119°	17	85°	20	147°
North Atlantic									
Gibraltar	36°08′N	5°21′W	1961–96	2.6	70°	9	26°	2	104°
Bermuda	32°22′N	64°42′W	1985–98	3.5	294°	4	320°	2	249°

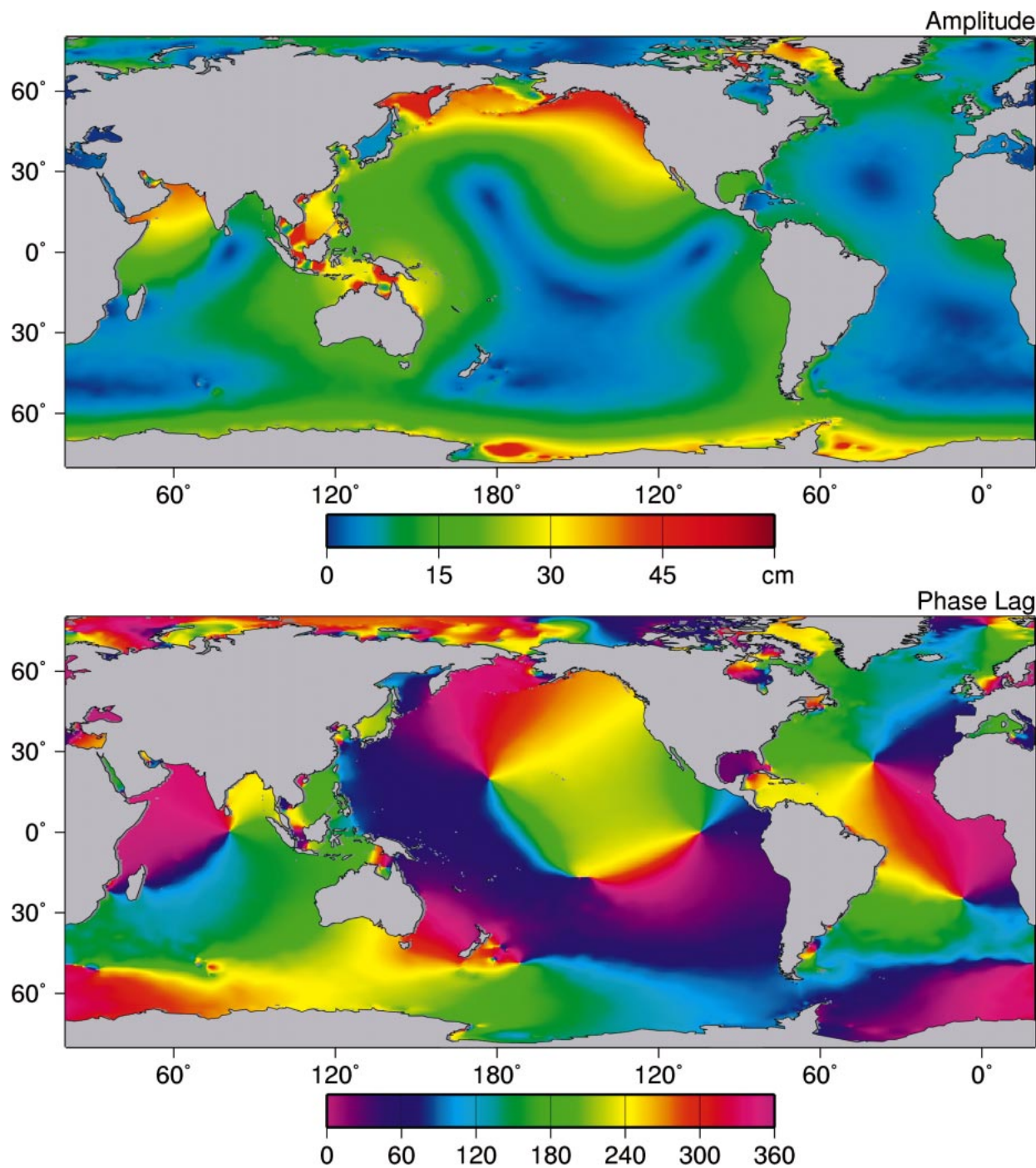* From Ponchaut et al. (2001). All others computed by the authors.

FIG. 6. (top) Amplitude and (bottom) Greenwich phase lags of the K$_1$ tide as determined from analysis of T/P altimetry, from Ray (1999).

where S_k is a "shape factor" that depends on the co-herence between the generating potential (a function of ω) and each mode k. We adopt the dissipationless modes of Platzman et al. (1981) for H_k. Being dissipationless each mode's eigenfrequency is a real number, s_k. Use of real frequencies directly in (3) would be highly unrealistic, however, and so we allow for dissipation by setting $\sigma_k = s_k(1 + i/2Q)$. For simplicity we take $Q = 10$ as being broadly representative of diurnal tides (e.g., Cartwright and Ray 1991). [Note that Platzman's (1984a) synthesis procedure was more sophisticated. For example, by employing perturbation methods, he allowed for dissipative effects in H_k and he devoted much effort to the specification of that dis-

sipation. However, again our goal here is insight, not realistic synthesis.]

According to (3) each mode contributes to the constituent $\zeta(\omega)$ according to its frequency and to its coherence with the generating potential. For $Q = 10$ the dependence on frequency is not especially sensitive; the coherence S_k is the dominating factor. We evaluate S_k by the surface integral

$$S_k = A^{-1} \iint_A H_k^* \overline{Z} \, dA \qquad (4)$$

over the ocean domain of area A, where $\overline{Z}$ is a complex equilibrium tide. For K_1 the tide $\overline{Z}$ is given by

$$\overline{Z}(\theta, \varphi) = \gamma_2 A_\omega Y_2^1(\theta, \varphi)$$
$$= \gamma_2 A_\omega \sqrt{(5/24\pi)} P_2^1(\cos\theta) e^{i\varphi},$$

where P_2^1 is the associated Legendre function, the amplitude A_ω is 36.9 cm for K_1, and γ_2 is a combination of Love numbers equaling approximately 0.736 at the K_1 frequency. For S_1 the equilibrium tide $\overline{Z}$ is given by

$$\overline{Z}(\theta, \varphi) = P(\theta, \varphi)/g\rho,$$

where P is the barometric tidal pressure depicted in Fig. 1. The modes H_k are normalized such that the total energy (potential plus kinetic) of each mode over the global ocean is constant.

The integral (4) has been evaluated for each of the 16 normal modes of Platzman et al. (1981) that lie between frequencies 0.6 and 1.7 cpd. The resulting spectral contribution of each mode to the K_1 and S_1 tides is shown in Fig. 7. As Platzman (1984b) found, K_1 is dominated by a single normal mode, that of period 28.7 h with a smaller contribution from a mode of period 21.2 h. Other gravitational tides in the diurnal band have similar spectral contributions, except that the single 28.7-h mode is usually even more pronounced since other major diurnal tides have periods closer to 28.7 h. In contrast, S_1 is a conglomeration of several modes, the largest of periods 25.7, 23.7, 17.7, and 21.2 h (in that order). The 17.7-h mode actually has the dominant shape factor S_k for S_1, but its contribution is reduced by the frequency factor in (3) relative to the first two modes, which are much closer to the S_1 frequency.

The five modes that compose the dominant contributions to the K_1 and S_1 tides are shown in Fig. 8. [Other modes in this frequency band can be found in the atlas of charts published by Platzman (1985).] All are predominantly gravity modes.

These five modes shed considerable light on the various characteristics of K_1 and S_1 that we have observed above. The Antarctic Kelvin wave, so conspicuous in K_1 (and in all major gravitational tides), arises primarily from the 28.7-h normal mode, which is minimally excited by the S_1 air tide. The 28.7-h mode also has relatively strong amplitudes in the North Pacific, as does the secondary K_1 mode at 21.2h. Tide S_1 is also energetic
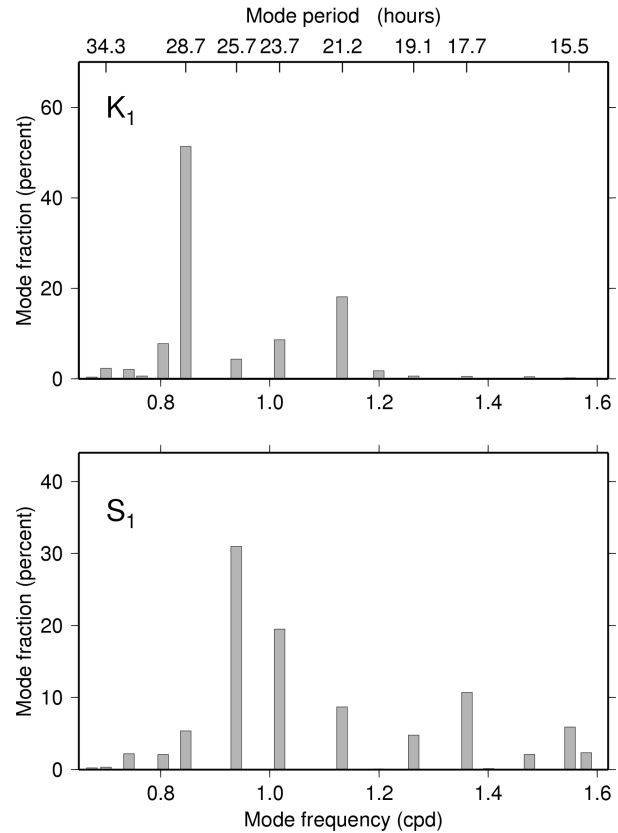

FIG. 7. Spectral composition of the K1 and S1 tides in terms of 16 near-diurnal normal modes of Platzman (1984) according to (3), in percentage units.

in the North Pacific, but it evidently owes this primarily to the 21.2-h mode alone. Unfortunately, Platzman's grid was not sufficiently fine to include the Okhotsk Sea, but we conjecture that both the 28.7- and 21.2-h modes are energetic there, as in Figs. 3, 4, and 6.

The two most energetic contributors to S_1—the 25.7- and 23.7-h modes—form an interesting couplet. The amplitudes of these modes are nearly identical except for the nodal region in the mid-Atlantic. They are both most intense in the northern North Atlantic, which is a region where S_1 is not especially large (excepting the Labrador Sea). Note, however, that the relative phases of the modes are aligned only in the North Atlantic and the modes are out of phase elsewhere. Because the air tide excites these two modes only in lower latitudes where they are out of phase, their expansion coefficients in (3) must be of nearly opposite sign, and this must cause near cancellation of the modes in the North Atlantic. The cancellation evidently fails in the Labrador Sea, where S_1 is surprisingly energetic, and also along the coast of Britain, but the modes are spatially too coarse to resolve either of those regions adequately.

The 17.7-h mode, which in terms of frequency is the farthest of the five modes from S_1, is primarily a transverse wave in the North Indian Ocean. It is apparently
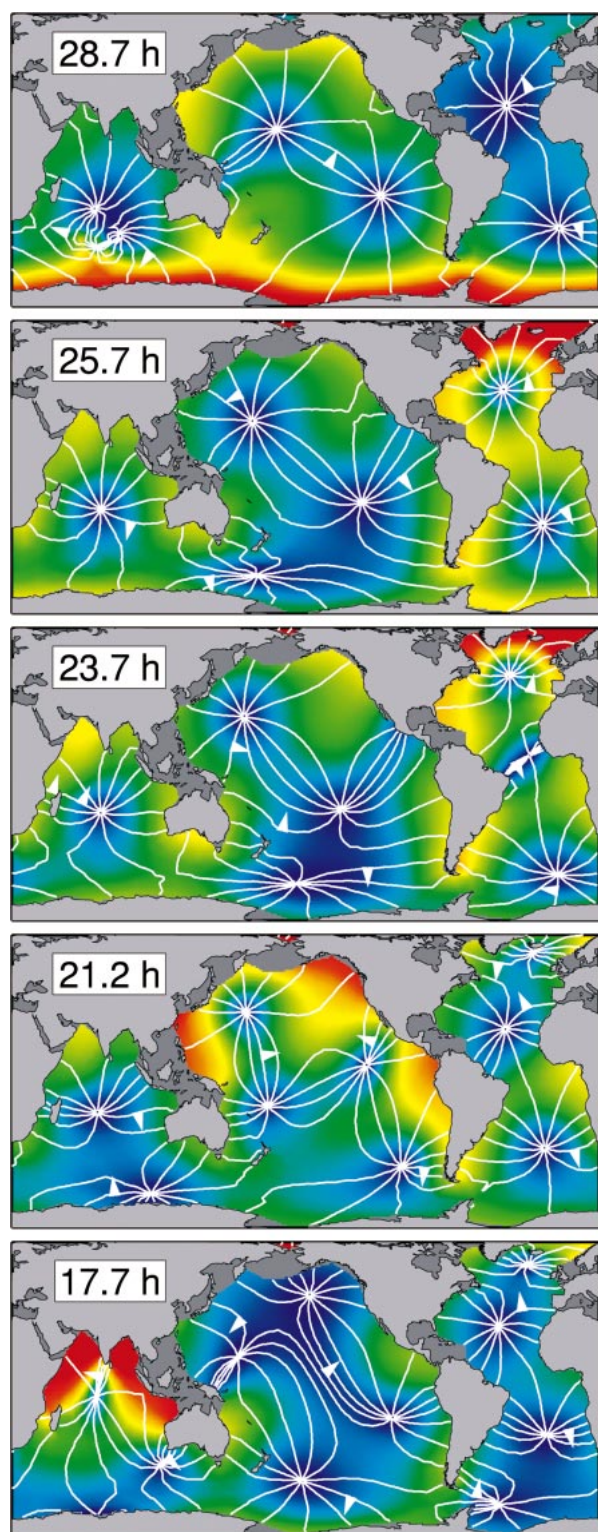
FIG. 8. Five oceanic normal modes, as determined by Platzman (1984), which constitute the dominant contributions to the K_1 and S_1 tides, according to Fig. 7. Colors denote amplitudes from small (dark blue) through large (dark red). Phases are contoured (white lines) every 30°, with direction of propagation indicated by the small arrows attached to the 0° contours.

highly coherent with the S_1 atmospheric tide, as Fig. 1 would suggest, to such extent that the mismatch in frequency is easily compensated for, hence producing large S_1 amplitudes in the Arabian Sea and relatively large currents throughout the entire Indian Ocean (Fig. 5). The 17.7-h mode also likely explains the large S_1 amplitudes northwest of Australia, although the normal-mode grid lacks sufficient resolution in the Indonesian region to be unambiguous on this point.

We conclude that the relative excitations of various normal modes, according primarily to their spatial coherence with the tidal forcing, explain most of the similarities and differences that we observe in the altimetric and modeled S_1 and K_1 tides.

7. Summary

Despite the high susceptibility of S_1 to systematic measurement errors, the degree of correspondence between altimetric estimates, tide-gauge point estimates, and hydrodynamic modeling leads us to believe that at least the gross features of the S_1 global tide have been captured in our Figs. 3 and 4. While less than 1 cm thoughout much of the global ocean, S_1 attains amplitudes of 2 cm in some regions, and 2 or 3 times that in certain isolated locations.

The relatively large S_1 amplitude in certain high-latitude regions is a striking example of the dynamic ocean response to diurnal pressure loading, since significant loading occurs without exception only in low-latitude regions. Other diurnal tides have, in some respects, similar high-latitude features (e.g., large amplitudes in the Okhotsk Sea and the Gulf of Alaska), but in these cases maximum equilibrium tide occurs at ±45°, not at the equator. It seems clear that the S_1 atmospheric tide, although confined to low latitudes, excites certain global oceanic normal modes, and like a lever struck on one side of its pivot, these modes respond throughout the global ocean. The one important diurnal mode that is evidently not easily excited by the air tide is the 28.7-h mode, which is the one mode primarily responsible for the Antarctic Kelvin wave that is observed in all other (gravitational) diurnal tides.

APPENDIX A

S_1 Phase Convention

Perhaps owing to the small size of the S_1 tide, several inconsistent phase conventions have developed and are in routine use, so some care must be exercised when interpreting published harmonic constants. One convention adopts the standard phase convention for gravitational diurnal tides, which entails adopting the phase of the largest spectral line in the constituent. In that case the S_1 equilibrium argument is (see section 2c)

$$T + p' + 90°,$$

where T is universal time and p' is the mean longitude of solar perihelion (and the 90° advance assumes a cosine argument; see Doodson 1928). This argument corresponds to the larger of the two primary lines in the S_1 constituent; see (1). In a tidal analysis, one would naturally employ all gravitational lines to determine the tidal admittance, implying an effective (present day) argument for the generating potential of (see section 2c)

$$T + 295.66° + 90°.$$

Foreman (1977) uses this convention in his widely used package.

American and British governmental agencies routinely follow Schureman (1940) and Doodson (1928), respectively, and fortunately in the case of S_1 their conventions are consistent. Both authors acknowledge the dominance of radiational forcing, as opposed to gravitational forcing, and they therefore employ the simple argument (again with cosine)

$$T + 180°,$$

so that the in-phase tidal component corresponds to times of maximum radiational forcing at Greenwich. See Table XXVII of Doodson (1928) and Table 2 of Schureman (1940). In this paper we follow the Doodson–Schureman convention. Hence, the cotidal phases of Figs. 1, 3, and 4 are relative to Greenwich noon.

APPENDIX B

S_1 Angular Momentum

Knowledge of the ocean tidal angular momentum is needed in certain studies of the earth's rotation rate, polar motion, and nutation. Our computed S_1 elevations and currents can be used directly to compute global angular momentum integrals following, for example, Seiler (1991) or Chao and Ray (1997). The results are summarized in Table B1. Note that because a diurnal-period wave appears as an annual-period wave when viewed from inertial space, the S_1 ocean tide perturbs the earth's (prograde) annual nutation. This particular nutation is well known for its mismatch between theory and observation (e.g., Dehant et al. 2003). The most advanced models of the annual nutation (Mathews et al.

TABLE B1. Global angular momentum integrals of S_1 ocean tide. All amplitudes are $\times 10^{23}$ kg m^2 s^{-1}.

	Mass terms		Motion terms	
	Amplitude	Phase lag	Amplitude	Phase lag
x	0.82	158°	1.72	14°
y	2.90	306°	1.62	226°
z	2.42	219°	2.57	271°

2002) assume that the S_1 ocean tide is either purely gravitational or purely isostatic with the air tide, neither of which is true, as we have seen in this paper. The angular momentum terms derived from these simplified theories should be augmented or replaced by the more realistic terms given in Table B1.

The phase lags in Table B1 follow the Doodson convention as in appendix A, and they are consistent with the phases shown in Fig. 4.

The values in Table B1 are computed from our hydrodynamic model, and they therefore do not include the gravitational part of S_1. The gravitational part can be easily inferred by admittance relationships from the angular momentum of the K_1 tide, tabulated by, for example, Chao et al. (1996).

REFERENCES

Accad, Y., and C. L. Pekeris, 1978: Solution of the tidal equations for the M_2 and S_2 tides in the World Ocean from a knowledge of the tidal potential alone. *Philos. Trans. Roy. Soc. London,* **A290,** 235–266.

Cartwright, D. E., and R. J. Tayler, 1971: New computations of the tide-generating potential. *Geophys. J. Roy. Astron. Soc.,* **23,** 45–74.

——, and A. C. Edden, 1973: Corrected tables of tidal harmonics. *Geophys. J. Roy. Astron. Soc.,* **33,** 253–264.

——, and R. D. Ray, 1991: Energetics of global ocean tides from Geosat altimetry. *J. Geophys. Res.,* **96,** 16 897–16 912.

Chao, B. F., and R. D. Ray, 1997: Oceanic tidal angular momentum and Earth's rotation variations. *Progress in Oceanography,* Vol. 40, Pergamon, 399–421.

——, ——, J. M. Gipson, G. D. Egbert, and C. Ma, 1996: Diurnal/semidiurnal polar motion excited by oceanic tidal angular momentum. *J. Geophys. Res.,* **101,** 20 151–20 163.

Chapman, S., and R. S. Lindzen, 1970: *Atmospheric Tides.* Reidel, 200 pp.

Dai, A., and C. Deser, 1999: Diurnal and semidiurnal variations in global surface wind and divergence fields. *J. Geophys. Res.,* **104,** 31 109–31 125.

——, and J. Wang, 1999: Diurnal and semidiurnal tides in global surface pressure data. *J. Atmos. Sci.,* **56,** 3874–3891.

Dehant, V., M. Feissel-Vernier, O. de Viron, C. Ma, M. Yseboodt, and C. Bizouard, 2003: Remaining error sources in the nutation at the submilliarc second level. *J. Geophys. Res.,* **108,** 2275, doi:10.1029/2002JB001763.

Deser, C., and C. A. Smith, 1998: Diurnal and semidiurnal variations of the surface wind field over the tropical Pacific Ocean. *J. Climate,* **11,** 1730–1748.

Dickinson, R. E., 1975: Meteorology of the upper atmosphere. *Rev. Geophys. Space Phys.,* **13,** 771–790.

Doodson, A. T., 1928: The analysis of tidal observations. *Philos. Trans. Roy. Soc. London,* **A227,** 223–279.

Egbert, G. D., and S. Y. Erofeeva, 2002: Efficient inverse modeling

of barotropic ocean tides. *J. Atmos. Oceanic Technol.,* **19,** 183–204.

——, R. D. Ray, and B. G. Bills, 2004: Numerical modeling of the global semidiurnal tide in the present day and in the last glacial maximum. *J. Geophys. Res.,* **109,** C03003, doi:10.1029/2003JC001973.

Forbes, J. M., 1982: Atmospheric tides 1. Model description and results for the solar diurnal component. *J. Geophys. Res.,* **87,** 5222–5240.

Foreman, M. G. G., 1977: Manual for tidal heights analysis and prediction (rev. 1996). Pacific Marine Science Rep. 77-10, Institute of Ocean Sciences, Victoria, BC, Canada, 58 pp.

Gordeev, R. G., B. A. Kagan, and E. V. Polyakov, 1977: The effects of loading and self-attraction on global ocean tides: The model and the results of a numerical experiment. *J. Phys. Oceanogr.,* **7,** 161–170.

Halpern, D., and R. K. Reed, 1976: Heat budget of the upper ocean under light winds. *J. Phys. Oceanogr.,* **6,** 972–975.

Haurwitz, B., and A. D. Cowley, 1973: The diurnal and semidiurnal barometric oscillations, global distribution and annual variation. *Pure Appl. Geophys.,* **102,** 193–222.

Hendershott, M. C., 1972: The effects of solid earth deformation on global ocean tides. *Geophys. J. Roy. Astron. Soc.,* **29,** 389–402.

Hsu, H.-H., and B. J. Hoskins, 1989: Tidal fluctuations as seen in ECMWF data. *Quart. J. Roy. Meteor. Soc.,* **115,** 247–264.

Kalnay, E., and Coauthors, 1996: The NCEP/NCAR 40-Year Reanalysis Project. *Bull. Amer. Meteor. Soc.,* **77,** 437–471.

Koblinsky, C. J., B. D. Beckley, R. D. Ray, Y.-M. Wang, L. Tsaoussi, A. Brenner, and R. Williamson, 1999: NASA Ocean Altimeter Pathfinder Project, report 1: Data processing handbook. NASA Tech. Memo. 208605, 55 pp.

Kowalik, Z., and I. Polyakov, 1998: Tides in the Sea of Okhotsk. *J. Phys. Oceanogr.,* **28,** 1389–1409.

Marshall, J. A., and S. B. Luthcke, 1994: Modeling radiation forces acting on TOPEX/Poseidon for precise orbit determination. *J. Spacecr. Rockets,* **31,** 89–105.

——, N. P. Zelensky, S. M. Klosko, D. S. Chinn, S. B. Luthcke, K. E. Rachlin, and R. G. Williamson, 1995: The temporal and spatial characteristics of TOPEX/Poseidon radial orbit error. *J. Geophys. Res.,* **100,** 25 331–25 352.

Mathews, P. M., T. A. Herring, and B. A. Buffett, 2002: Modeling of nutation and precession: New nutation series for nonrigid Earth and insights into the earth's interior. *J. Geophys. Res.,* **107,** 2068, doi: 10.1029/2001JB000390.

Munk, W. H., and D. E. Cartwright, 1966: Tidal spectroscopy and prediction. *Philos. Trans. Roy. Soc. London,* **259,** 533–581.

Pattiaratchi, C., B. Hegge, J. Gould, and I. Eliot, 1997: Impact of sea-breeze activity on nearshore and foreshore processes in southwestern Australia. *Cont. Shelf Res.,* **17,** 1539–1560.

Platzman, G. W., 1984a: Normal modes of the World Ocean. Part III. A procedure for tidal synthesis. *J. Phys. Oceanogr.,* **14,** 1521–1531.

——, 1984b: Normal modes of the World Ocean. Part IV: Synthesis of diurnal and semidiurnal tides. *J. Phys. Oceanogr.,* **14,** 1532–1550.

——, 1985: Normal modes of the World Ocean: Maps and tables. University of Chicago, Dept. Geophysical Sciences, 97 pp.

——, 1991: Tidal evidence for ocean normal modes. *Tidal Hydrodynamics,* B. B. Parker, Ed., John Wiley and Sons, 13–26.

——, G. A. Curtis, K. S. Hansen, and R. D. Slater, 1981: Normal modes of the World Ocean. Part II: Description of modes in the period range 8 to 80 hours. *J. Phys. Oceanogr.,* **11,** 579–603.

Ponchaut, F., F. Lyard, and C. Le Provost, 2001: An analysis of the tidal signal in the WOCE sea level dataset. *J. Atmos. Oceanic Technol.,* **18,** 77–91.

Ponte, R. M., and R. D. Ray, 2002: Atmospheric pressure corrections in geodesy and oceanography: A strategy for handling air tides. *Geophys. Res. Lett.,* **29,** 2153.

Quartley, G. D., T. H. Guymer, and M. A. Srokosz, 1996: The effects of rain on TOPEX radar altimeter data. *J. Atmos. Oceanic Technol.,* **13,** 1209–1229.

Ray, R. D., 1998: Diurnal oscillations in atmospheric pressure at twenty-five small oceanic islands. *Geophys. Res. Lett.,* **25,** 3851–3854.

——, 1999: A global ocean tide model from TOPEX/Poseidon altimetry: GOT99. 2. NASA Tech. Memo. 209478, 58 pp.

——, and R. M. Ponte, 2003: Barometric tides from ECMWF operational analyses: *Ann. Geophys.,* **21,** 1897–1910.

Schrama, E. J. O., and R. D. Ray, 1994: A preliminary tidal analysis of TOPEX/Poseidon altimetry. *J. Geophys. Res.,* **99,** 24 799–24 808.

Schureman, P., 1940: *Manual of Harmonic Analysis and Prediction of Tides.* U.S. Government Printing Office, 317 pp.

Seiler, U., 1991: Periodic changes of the angular momentum budget due to the tides of the World Ocean. *J. Geophys. Res.,* **96,** 10 287–10 300.

Simon, J. L., P. Bretagnon, J. Chapront, M. Chapront-Touze, G. Francou, and J. Laskar, 1994: Numerical expressions for precession formulae and mean elements for the Moon and the planets. *Astron. Astrophys.,* **282,** 663–683.

Soden, B. J., 2000: The diurnal cycle of convection, clouds, and water vapor in the tropical upper troposphere. *Geophys. Res. Lett.,* **27,** 2173–2176.

Vial, F., F. Lott, and H. Teitelbaum, 1994: A possible signal of the El Niño–Southern Oscillation in time series of the diurnal tide. *Geophys. Res. Lett.,* **21,** 1603–1606.

Wood, R., C. S. Bretherton, and D. L. Hartmann, 2002. Diurnal cycle of liquid water path over the subtropical and tropical oceans. *Geophys. Res. Lett.,* **29,** 2092, doi: 10.1029/2002GL015371.

Wunsch, C., and D. Stammer, 1995: The global frequency-wavenumber spectrum of oceanic variability estimated from TOPEX/Poseidon altimetric measurements. *J. Geophys. Res.,* **100,** 24 895–24 910.